A reversal in global terrestrial stilling and its implications for wind energy production

Zhenzhong Zeng, Alan D Ziegler, Timothy Searchinger, Long Yang, Anping Chen, Kunlu Ju, Shilong Piao, Laurent Li, Philippe Ciais, Deliang Chen, et al.

Accepted manuscript for Nature Climate Change, Zeng et al. 2019, https://doi.org/10.1038/s41558-019-0622-6

A reversal in global terrestrial stilling and its implications for wind energy production

Zhenzhong Zeng[1,2]*, Alan D. Ziegler[3], Timothy Searchinger[4], Long Yang[5], Anping Chen[6], Kunlu Ju[7], Shilong Piao[8], Laurent Z. X. Li[9], Philippe Ciais[10], Deliang Chen[11], Junguo Liu[2], Cesar Azorin-Molina[11,12], Adrian Chappell[13], David Medvigy[14], Eric F. Wood[1]

[1] Department of Civil and Environmental Engineering, Princeton University, Princeton, New Jersey 08544, USA

[2] School of Environmental Science and Engineering, South University of Science and Technology, Shenzhen 518055, China

[3] Geography Department, National University of Singapore, 1 Arts Link Kent Ridge, Singapore 117570, Singapore

[4] Woodrow Wilson School, Princeton University, Princeton, New Jersey 08544, USA

[5] School of geography and ocean science, Nanjing University, Nanjing, Jiangsu Province, China

[6] Forestry and Natural Resources, Purdue University, West Lafayette, Indiana 47907, USA

[7] School of Economics and Management, Tsinghua University, Beijing 100084, China

[8] Sino-French Institute for Earth System Science, College of Urban and Environmental Sciences, Peking University, Beijing 100871, China

[9] Laboratoire de Météorologie Dynamique, CNRS, Sorbonne Université, Ecole Normale Supérieure, Ecole Polytechnique, 75252 Paris, France

[10] Laboratoire des Sciences du Climat et de l'Environnement, UMR 1572 CEA-CNRS-UVSQ, 91191 Gif-sur-Yvette, France

[11] Regional Climate Group, Department of Earth Sciences, University of Gothenburg, Gothenburg, Sweden

[12] Centro de Investigaciones sobre Desertificación, Consejo Superior de Investigaciones Cientificas (CIDE-CSIC), Montcada, Valencia, Spain

[13] School of Earth and Ocean Sciences, Cardiff University, Wales, CF10 3AT, UK

[14] Department of Biological Sciences, University of Notre Dame, Notre Dame, IN 46556, USA

*Correspondence to: zzeng@princeton.edu

Manuscript for *Nature Climate Change*

September 01, 2019

Wind power, a rapidly growing alternative energy source, may be threatened by reductions in global average surface wind speed over land since the 1980s, known as terrestrial stilling. However, this stilling is largely unexplained so far. Here we use wind data from *in-situ* stations worldwide to show that the stilling reversed around 2010 and global wind speeds over land have recovered. We illustrate that decadal-scale variations of near-surface wind are likely dertermined by internal decadal ocean/atmosphere oscillations, rather than the previous hypothesis of vegetation growth and/or urbanization. The strengthening has increased potential wind energy by 17 ±2% for 2010-2017, increasing U.S. wind power capacity factor by ~2.5% that is as significant as technology innovations. In the longer-term, use of ocean/atmosphere oscillations to anticipated future wind speeds, could allow optimization of turbines for expected speeds during their productive life spans.

Reports of a global decline in land surface wind speed of 8% from ~1980 to 2010 have raised concerns about outputs from future wind power[1-5]. Wind power (p) varies with the cube of wind speed (u) according to the formula

$$p = \frac{\rho s f}{2} u^3 \quad (1),$$

where ρ is air density, s the swept area of the turbine, and f an efficiency factor[6]. The decline has been manifest in the northern mid-latitude countries where the majority of wind turbines are installed including China, the U.S. and Europe[1]. If the observed trend from 1980 to 2010 were to continue to the end of the century, global u would reduce by 21%, halving the amount of power available in the wind (using Equation (1)). Understanding the drivers of this long-term decline in wind speed is critical not merely to maximize wind energy production[7-9] but also to address other globally significant environmental problems related to stilling, including reduced aerosol

dispersal, changes in evapotranspiration rates, and adverse effects on animal behavior and ecosystem functioning[1,3,4,10].

The potential causes for global terrestrial stilling are complex and remain contested[2,3,11,12]. Many regional-scale studies[13-15G&W] using reanalysis datasets have found correlations of *u* with various climate indices. Those studies hypothesize that terrestrial stilling is caused by decreased driving force due to the change in large scale circulations[11]. This is supported by a consistency in wind speed changes at the surface and at higher levels in the reanalysis datasets[11,14]. Nevertheless, there are large uncertainties in these datasets[2,11,14], and more importantly, global terrestrial stilling is either not reproduced or has been largely underestimated in global reanalysis products[2,11] (Supplementary Fig. 1) and/or climate model simulations for IPCC AR5 (Supplementary Fig. 2). Acknowledging that wind speed reanalysis datasets do not represent land surface dynamics, the discrepancies between the decreasing trends derived from *in-situ* stations and from reanalysis or climate model simulations lead to the hypothesis that global terrestrial stilling is caused by increased drag related to increased surface roughness from the greening of the Earth and/or urbanization[2,16], both of which would suggest further future declines.

However, conversely, recent studies have described wind speed reversal at local scales[17,18] or an increase of global wind speed during a particular year[19], despite uncertainty over the global trend of wind speed change[5,11]. The recent reversal over land, if evidenced to be true at global scale, could elucidate the causes of global terrestrial stilling and potentially improve future wind energy projections.

Analysis

We integrate direct *in-situ* observations of *u* from ground weather stations from 1978 to 2017 together with statistical models for detection of trends. The stations, mainly distributed in the northern mid-latitudes countries, were carefully selected from the Global Summary of Day (GSOD) database following strict quality control procedures (Supplementary Fig. 3; see *Methods* for details). To test for a continuation of the terrestrial stilling after 2010 (refs 1-3), we use a piecewise linear regression model to examine the potential trend changes[26,27].

Scope of a reversal in global terrestrial stilling

The analysis shows that global mean annual *u* decreased significantly at a rate of -0.08 m s^{-1} (or -2.3%) per decade during the first three decades beginning in 1978 (P-value < 0.001; Fig. 1a, Supplementary Table 1). While the decreasing trend has previously been shown[2-4] and confirms global terrestrial stilling as an established phenomenon during the period of 1978-2010, we find that *u* has significantly increased in the current decade. This turning point is statistically significant at $P < 0.001$ with a goodness of fit of an $R^2 = 90\%$ (Fig. 1a). The recent increasing rate of 0.24 m s^{-1} $decade^{-1}$ ($P < 0.001$) is three-fold the decreasing rate before the turning point in 2010.

To exclude the possibility that the turning point is caused by large wind speed changes at only a few sites, we repeat our analyses 300 times by randomly resampling 40% of the global stations each time (grey lines in Fig. 1a; 40% of the stations are selected to ensure a sufficient sample size ($n > 500$)). We find significant turning points in each randomly-selected sub-sample ($P < 0.001$; $R^2 \geq 76\%$). Run-specific turning points occur between 2002 and 2011, with most (95%) of

them between 2009 and 2011 (Fig. 1b). In addition, mean annual *u* changes before and after a specific turning point based on the 300 sub-sample estimates are -0.08 ± 0.01 m s^{-1} per decade and 0.24 ± 0.03 m s^{-1} per decade, respectively (Fig. 1c), identical to those values based on all the global samples.

Spatial analyses further confirm that the recent reversal is a global-scale phenomenon (Supplementary Fig. 4a-c). A majority (79%) of the stations where *u* decreased significantly during 1978-2010 (Supplementary Fig. 4b) have positive trends in *u* after 2010 (Supplementary Fig. 4c). The stations are mainly distributed over North America, Europe, and Asia. Significant turning points exist in all the three regional mean annual *u* time series ($P < 0.001$, Supplementary Fig. 4d-f), but they vary in the specific year of occurrence. For example, a turning point occurs earlier in Asia (2001, R^2 =80%, Supplementary Fig. 4f) and Europe (2003, R^2 = 56%, Supplementary Fig. 4e) than in North America (2012, R^2 = 80%, Supplementary Fig. 4d). Nevertheless, all the three regions have the most significant increase in *u* after ~2010 (Supplementary Fig. 4d-f).

The existence of turning points is robust regardless of season (Supplementary Table 1 and Supplementary Fig. 5) or wind variable chosen for analysis (Supplementary Fig. 6), and shows no dependence on quality control procedures for weather station data (Supplementary Fig. 7). For maximum sustained wind and wind gusts, the turning points appear earlier and the recent increasing rates are weaker (Supplementary Fig. 6). Furthermore, we show that our findings are robust and repeatable (Supplementary Fig. 8) using a different data set—the HadISD database, which follows station selection criteria and a suite of quality control tests established by Met

Office Hadley Centre[28]. We also find that the tendency for an increasing number of stations becoming automated during recent decades (Supplementary Figs 9 and 10) does not affect the result (Supplementary Fig. 11). Finally, to test the effect of inhomogeneity, we remove all the stations with change points detected by the Pettitt tests[29], finding that the reults do not change after the analysis is repeated (Supplementary Fig. 12). All these lines of evidences provide independent supports that the trends in *u* are not caused by changes in measurement methods and inhomogeneity.

Causes of the reversal in global terrestrial stilling

A variety of theories have been presented previously to explain stilling, many of which focus on the drag force of *u* linked to increased terrestrial roughness caused by urbanization and/or vegetation changes[2,12]. These theories have been disputed[30] (also see Supplementary Figs 13 and 14). Our finding that global stilling changed after 2010, especially the increasing rate which is three times that of the decreasing rate before 2010 (Fig. 1a), further refutes these theories because terrestrial roughness did not suddenly change in 2010. More likely, the variation in *u* (including prior stilling and the recent reversal) is determined mainly by driving forces associated with decadal variability of large-scale ocean/atmospheric circulations.

Wind is physically created by pressure gradient which is due to uneven heating of the Earth surface (temperature anomalies or heterogeneity), and the latter is to a large extent described by climate indices for oscillations. To test such associations, we first include twenty-one climate indices in the pool of indicators for ocean/atmosphere oscillations (Supplementary Table 2 and *Methods*). To avoid overfitting, we apply stepwise regression[32] to identify six largest explanatory

power factors for the decadal variations of *u* over the globe, North America, Europe, and Asia, respectively (see Supplementary Table 3). The reconstructed *u* obtained from the stepwise linear regression matches well with the observed *u* (Supplementary Figs 15 and 16, and discussion in *Methods*). Finally, we train our models only using the detrended time series before the turning points (2010 for the globe, 2012 for North America, 2003 for Europe, and 2001 for Asia), finding that the models are capable of reproducing the positive trends after the turning points, not only for the globe ($P < 0.001$; Fig. 2a), but also for all the three regions ($P < 0.001$; Fig. 2b-d). The magnitude of the increasing rate after the turning points is well modelled (Fig. 2). These results suggest a predictive relationship between wind changes and ocean/atmosphere oscillations, which would be very valuable for the wind energy sector.

To uncover the mechanisms behind the decadal variations of *u*, we construct the composite annual mean surface temperature for the years that exhibit negative (Fig. 3a) and positive (Fig. 3b) anomalies of detrended *u*. During the years of negative *u* anomalies (Fig. 3a) the following are observed: (a) positive anomalies of temperature prevail over the Tropical Northern Atlantic (TNA region, 5.5^{o}N to 23.5^{o}N, 15^{o}W to 57.5^{o}W), showing a positive value for Tropical Northern Atlantic Index (TNA); (b) the west (east) Pacific is warmer (colder) than normal years, demonstrating a negative value for Pacific Decadal Oscillation (PDO); and (c) positive anomalies of temperature occur near the Azores and negative anomalies occur over Greenland, indicating a negative value for North Atlantic Oscillation (NAO). The opposite pattern (i.e. negative TNA, positive PDO and NAO) occurs during the years of positive *u* anomalies (Fig. 3b). Furthermore, TNA has strong, significant, and negative correlations with regional *u*, in particular, over North America (Fig. 3c). PDO has significant positive correlations with regional *u* globally (Fig. 3e).

NAO has overwhelmingly significant positive correlations with regional *u* in the U.S. and Northern Europe, but negative correlation with regional *u* in Southern Europe (Fig. 3d). These patterns are consistent with the finding that the greatest explanatory power factor is TNA for North America ($R = -0.67$, $P < 0.001$), PDO for Asia ($R = 0.50$, $P < 0.01$), and NAO for Europe ($R = 0.37$, $P < 0.05$) (more discussions refer to *Methods*). The ocean/atmosphere oscillations, characterized as the decadal variations in these climate indices (mainly TNA, NAO, PDO), can therefore explain the decadal variation of *u* (i.e., the long-term stilling and the recent reversal) (Figs 2 and 3f-h).

There are some theories[20-23] for potential physical mechanisms how these oscillations affect regional *u* over land. With respect to TNA, prior studies demonstrate that the positive phase of TNA is linked with a weakened Hadley circulation (more details refer to ref. 21). During the positive phase of TNA there is a cold anomaly over the eastern coast of the U.S. (Fig. 3a and ref. 21). This pattern leads to a southward component of surface wind and a stable environment of weak convergence from the tropics to the mid-latitudes, resulting a reduction of *u* in the mid-latitudes, the U.S. in particular (Fig. 3c and Supplementary Fig. 17a,b). As for NAO, its negative and positive phases have different jet stream configurations and wind systems in Northern versus Southern Europe (Supplementary Fig. 17c,d; details refer to ref. 20). During the positive (negative) phase, the pressure gradient across the North Atlantic[20] generates strong winds and storms across Northern (Southern) Europe (Supplementary Fig. 17c,d), explaining the contrasting correlations of NAO to *u* in Northern and Southern Europe (Fig. 3d, Supplementary Fig. 18). For PDO, the temperature gradient during the negative (positive) phase generates an easterly (westerly) component of surface wind (details refer to refs 22, 23), which weakens

(strengthens) the prevailing westerly winds in the mid-latitudes (Supplementary Fig. 17e,f) and explains the widespread and significant positive correlations between PDO and *u* across the whole mid-latitudes (Fig. 3e). However, despite these potential physical mechanisms[20-23], the relationships between these oscillations and long-term wind speeds over land are still uncertain and require more investigations.

Finally, it is critical to determine why global reanalysis products do not reproduce or underestimate the historical terrestrial stilling (Supplementary Fig. 1), which is a major basis for the previous studies[2,12] rejecting the ocean/atmosphere oscillations as a dominant driver for terrestrial stilling. Global reanalysis products are generated at numerical weather prediction centers with their most-advanced data assimilation systems. But most of them cannot properly assimilate near-surface winds over land due to inappropriate model topography and inaccuarency of atmospheric boundary layer processes implemented into the data assimilation systems. ERA-Interim[35], one of the best products available, can only assimilate surface winds over seas from scatterometers, ships and bouys. The capacities of these products in reproducing the near-surface wind speed over land are thus generally poor and rely on climate models. We find that in the regions where AMIP model simulations (i.e. atmospheric simulations forced with observed sea surface temperature) capture the stilling, such as Europe and India (Fig. 4a,b in ref. 30), the global reanalysis products are also capable of reproducing the stilling in these regions (Fig. S1c); while in regions where AMIP simulations do not capture the stilling, such as North America[30,36], the global reanalysis products also fail to reproduce the stilling[2,11] (Fig. S1b). Therefore, it is the model limitations that prevent global reanalysis products from reproducing the observed near-surface wind speed changes in some regions satisfactorily. More efforts are required to improve

surface process parameterization scheme and its connection to ocean/atmosphere circulations in climate models and operational weather data assimilation systems.

Implications for wind energy production

In wind power assessments, near-surface wind observations from weather stations (u at the height of z_r = 10 meters) are often used to estimate wind speeds at the height of a turbine (u_{tb} at the height of z_{tb} = 50-150 meters) using an exponential wind profile power law relationship:

$$u_{tb} = u\left(\frac{z_{tb}}{z_r}\right)^{\alpha} \quad (2)$$

where the α is commonly assumed to be constant (1/7) in wind resource assessments because the differences between these two levels are unlikely great enough to introduce considerable errors in the estimates[5].

Changes in wind speed matter not only on average but also in the percentage of time wind speeds are high or low. A $u_{tb} > 3$ m s^{-1} is a typical minimum velocity needed to drive turbines efficiently, so wind speeds below 3 m s^{-1} are typically wasted from the power generation perspective. Although periods of high wind speed greatly increase the physical capacity to generate power according to formula (1), turbines are built with a maximum capacity, so periods of high wind speed can also "waste" the uses of wind with the threshold depending on the capacity of the turbine.

On average, the increase of global mean annual u from 3.13 m s^{-1} in 2010 to 3.30 m s^{-1} in 2017 (Fig. 1a; see *Methods* for details) increases the amount of energy entering a hypothetical wind

turbine receiving the global average wind by 17 ±2% (uncertainty is associated with subsamples in Fig. 1a; regionally, 22 ±2% for North America, 22 ±4% for Europe, and 11 ±4% for Asia). At the hourly scale, the frequency of low *u* decreases while the frequency of high *u* increases (Fig. 4a). Using one General Electric GE 2.5 – 120 turbine[37] (Supplementary Fig. 19) to illustrate, the effects of changes in global average *u* increase potential power generation from 2.4 million kWh in 2010 to 2.8 million kWh in 2017 (+17%). If the present trend persists for at least another decade, in the light of the robust increasing rate during 2000-2017 (Fig. 1a) and the long cycles of natural ocean/atmosphere oscillations[20-24] (Supplementary Fig. 20), power would rise to 3.3 million kWh in 2024 (+37%), resulting in a +3% per decade increase of global-average capacity factor (mean power generated divided by rated peak power) on average. This change is even larger than the projected change in wind power potential caused by climate change under multi-scenairos[38].

During the past decade, the capacity factor of the U.S. wind fleet[39] has steadily risen at a rate of +7% per decade (Fig. 4b), previously attributed solely to technology innovations[40]. We find that the capacity factor for wind generation in the U.S. is highly and significantly correlated with the variation in the cube of regional-average *u* (u^3, R = 0.86, P < 0.01; Fig. 4b). To isolate the *u*-induced increase in capacity factor from that due to technology innovations, we use the regional mean hourly wind speed in 2010 and 2017 to estimate the increase of capacity factor for a given turbine, thereby controlling for technology innovations. It turns out that the increased u^3 explains ~50% of the increase of the capacity factor (see *Methods* for details). Therefore, in addition to technology innovations, the strengthening *u* is another key factor powering the increasing

reliability of wind power in the U.S. (and other mid-latitude countries where *u* is increasing, such as China and European countries).

To illustrate the consequences, one turbine (General Electric GE 1.85 – 87 (ref. 41)) installed at one of our *in-situ* weather stations in the U.S. in 2014 (inset plot in Fig. 4c), which was expected to produce 1.8 ±0.1 million kWh using four years of *u* records before the installation (2009-2013)[41], actually produced 2.2 ±0.1 million kWh between 2014-2017 (+25%). This system has the potential to generate 2.8 ±0.1 million kWh (+56%) if *u* recovers to the 1980s level (red bars in Fig. 4d; see *Methods* for details). Globally, 90% of the global cumulative wind capacity has been installed in the last decade[25], during which global *u* has been increasing (see above).

Discussion

Although the response of ocean/atmosphere oscillations to anthropogenic warming remains unclear[23], the increases in wind speeds should continue for at least a decade because these oscillations change over decadal time frames[20-24]. Climate model simulations constrained with historical sea surface temperature also show a long cycle in *u* over land (Supplementary Fig. 20). Our findings are therefore good news for the power industry for the near future.

However, oscillation patterns in the future will likely cause returns to declining wind speeds, and anticipating these changes should be important for the wind power industry. Wind farms should be constructed in the areas with stable winds and high effective utilization hours (e.g. 3 - 25 m s^{-1}). If high wind speeds are likely to be common, building turbines with larger capacities could be justified. For example, capturing more available wind energy (blue bars in Fig. 4d) could be

achieved through the installation of higher capacity wind turbines (e.g. General Electric GE 2.5 – 120, green bars in Fig. 4d), greatly increasing total power generation. Most turbines tend to require replacement after 12-15 years[42]. Further refinement of the relationships uncovered in this paper could allow choices of turbine capacity, rotor and tower that are optimized not just to wind speeds of the recent past but to likely future changes during the lifespan of the turbines.

In summary, we find that after several decades of global terrestrial stilling, wind speed has rebounded, increasing rapidly in the recent decade globally since 2010. Ocean/atmosphere oscillations, rather than increased surface roughness, are likely the causes. These findings are important for those vested in maximizing the potential of wind as an alternative energy source. The development of renewable energy sources including wind power[6-9,25] is central to energy scenarios[8] that help keep warming well below 2 ◦C. One megawatt (MW) of wind power reduces 1,309 tonnes of CO_2 emissions and also saves 2,000 liters of water compared with other energy sources[9,25]. Since its debut in the 1980s, the total global wind power capacity reached 539 gigawatts by the end of 2017, and the wind power industry is still booming globally. For instance, the total wind power capacity in the U.S. alone is projected to increase fourfold by 2050 (ref. 9). The reversal in global terrestrial stilling bodes well for the expansion of large-scale and efficient wind power generation systems in these mid-latitude countries in the near future.

References.

1. Roderick, M. L., Rotstayn, L. D., Farquhar, G. D. & Hobbins, M. T. On the attribution of changing pan evaporation. *Geophys. Res. Lett.* **34,** 1–6 (2007).

2. Vautard, R., Cattiaux, J., Yiou, P., Thépaut, J. N. & Ciais, P. Northern Hemisphere atmospheric stilling partly attributed to an increase in surface roughness. *Nat. Geosci.* **3,** 756–761 (2010).

3. Mcvicar, T. R., Roderick, M. L., Donohue, R. J. & Van Niel, T. G. Less bluster ahead? ecohydrological implications of global trends of terrestrial near-surface wind speeds. *Ecohydrology* **5,** 381–388 (2012).

4. McVicar, T. R. *et al.* Global review and synthesis of trends in observed terrestrial near-surface wind speeds: Implications for evaporation. *J. Hydrol.* **416–417,** 182–205 (2012).

5. Tian, Q., Huang, G., Hu, K. & Niyogi, D. Observed and global climate model based changes in wind power potential over the Northern Hemisphere during 1979–2016. *Energy* **167,** 1224–1235 (2019).

6. Lu, X., McElroy, M. B. & Kiviluoma, J. Global potential for wind-generated electricity. *Proc. Natl. Acad. Sci.* **106,** 10933–10938 (2009).

7. UNFCCC. *Adoption of the Paris Agreement* (FCCC/CP/2015/L.9/Rev.1., 2015).

8. IPCC. *Summary for policymakers in Climate change 2014: Mitigation of climate change. Contribution of working group III to the fifth assessment report of the Intergovernmental Panel on Climate Change* (O. Edenhofer et al., Eds., Cambridge University Press, Cambridge, UK and New York, USA, 2014).

9. U.S. Department of Energy. *Projected growth wind industry now until 2050* (Washington, D.C., 2018).

10. Nathan, R. & Muller-landau, H. C. Spatial patterns of seed dispersal, their determinants and consequences for recruitment. *Trends Ecol. Evol.* **15,** 278–285 (2000).

11. Torralba, V., Doblas-Reyes, F. J. & Gonzalez-Reviriego, N. Uncertainty in recent near-surface wind speed trends: a global reanalysis intercomparison. *Environ. Res. Lett.* **12,** 114019 (2017).

12. Wu, J., Zha, J. L., Zhao, D. M. & Yang, Q. D. Changes in terrestrial near-surface wind speed and their possible causes: an overview. *Clim. Dyn.* **51,** 2039–2078 (2018).

13. Nchaba, T., Mpholo, M. & Lennard, C. Long-term austral summer wind speed trends over southern Africa. *Int. J. Climatol.* **37,** 2850–2862 (2017).

14. Chen, L., Li, D. & Pryor, S. C. Wind speed trends over China: quantifying the magnitude and assessing causality. *Int. J. Climatol.* **33,** 2579–2590 (2013).

15. Naizghi, M. S. & Ouarda, T. B. Teleconnections and analysis of long-term wind speed variability in the UAE. *Int. J. Climatol.* **37,** 230–248 (2017).

16. Zhu, Z. *et al.* Greening of the Earth and its drivers. *Nat. Clim. Chang.* **6,** 791–796 (2016).

17. Kim, J. C. & Paik, K. Recent recovery of surface wind speed after decadal decrease: a focus on South Korea. *Clim. Dyn.* **45,** 1699–1712 (2015).

18. Azorin-Molina, C. *et al.* Homogenization and assessment of observed near-surface wind speed trends over Spain and Portugal, 1961-2011. *J. Clim.* **27,** 3692–3712 (2014).

19. Tobin, I., Berrisford, P., Dunn, R. J. H., Vautard, R. & McVicar, T. R. [Global climate; Atmospheric circulation] Surface winds [in "State of the Climate in 2013". *Bull. Am. Meteorol. Soc.* **95,** S28-S29 (2014).

20. Hurrell, J. W., Kushnir, Y., Ottersen, G. & Visbeck, M. *The North Atlantic Oscillation climatic significance and environmental impact* (eds. Hurrell, J. W., Kushnir, Y., Ottersen, G. &

Visbeck, M., 2003).

21. Wang, C. Z. Atlantic climate variability and its associated atmospheric circulation cells. *J. Clim.* **15,** 1516–1536 (2002).

22. Zhang, Y., Xie, S.-P., Kosaka, Y. & Yang, J.-C. Pacific decadal oscillation: Tropical Pacific forcing versus internal variability. *J. Clim.* **31,** 8265–8279 (2018).

23. Timmermann, A. *et al.* El Niño-Southern Oscillation complexity. *Nature* **559,** 535–545 (2018).

24. Steinman, B. A. *et al.* Atlantic and Pacific multidecadal oscillations and Northern Hemisphere temperatures. *Science* **347,** 988-991(2015).

25. Global Wind Energy Council. *Global Wind Energy Outlook 2018* (2018).

26. Toms, J. D. & Lesperance, M. L. Piecewise regression: a tool for identifying ecological thresholds. *Ecology* **84,** 2034–2041 (2003).

27. Ryan, S. E. & Porth, L. S. *A tutorial on the piecewise regression approach applied to bedload transport data* (2007).

28. Dunn, R. J. H., Willett, K. M., Morice, C. P. & Parker, D. E. Pairwise homogeneity assessment of HadISD. *Clim. Past* **10,** 1501–1522 (2014).

29. Pettitt A. N. A non-parametric approach to the change-point problem. *J. R. Stat. Soc. Ser. C: Appl. Stat.* **28,** 126–135 (1979).

30. Zeng, Z. *et al.* Global terrestrial stilling: does Earth's greening play a role? *Environ. Res. Lett.* **13,** 124013 (2018).

31. Held, I. M., Ting, M. & Wang, H. Northern winter stationary waves: Theory and modeling. *J. Clim.* **15,** 2125–2144 (2002).

32. Draper, N. R. & Smith, H. *Applied Regression Analysis, 3rd Edition* (Wiley-Interscience,

1998).

33. Granger, C. W. J. Investigating causal relations by econometric models and cross-spectral methods. *Econometrica* **37,** 424–438 (1969).

34. Henriksson, S. V. Interannual oscillations and sudden shifts in observed and modeled climate. *Atmos. Sci. Lett.* **19,** e850 (2018).

35. Dee, D. P. *et al.* The ERA-Interim reanalysis: configuration and performance of the data assimilation system. *Q J. Roy. Meteor Soc.* **137,** 553–597 (2011).

36. Pryor, S. C. *et al*. Wind speed trends over the contiguous USA. *J. Geophys. Res. D: Atmos.* **114,** D14105 (2009).

37. Wind-turbine-models.com. General Electric GE 2.5 - 120. (2018). at https://www.en.wind-turbine-models.com/turbines/310-general-electric-ge-2.5-120

38. Tobin, I. *et al.* Climate change impacts on the power generation potential of European mid-century wind farms scenario. *Environ. Res. Lett.* **11,** 034013 (2016).

39. U.S. Energy Information Administration. Capacity factors for utility scale generators not primarily using fossil fuels, January 2013-August 2018. (2018). at https://www.eia.gov/electricity/monthly/epm_table_grapher.php?t=epmt_6_07_b

40. Dell, J. & Klippenstein, M. Wind Power Could Blow Past Hydro's Capacity Factor by 2020. (2018). at <https://www.greentechmedia.com/articles/read/wind-power-could-blow-past-hydros-capacity-factor-by-2020>

41. Wind-turbine-models.com. General Electric GE 1.85 - 87. (2018). at https://www.en.wind-turbine-models.com/turbines/745-general-electric-ge-1.85-87

42. Hughes, G. *The Performance of Wind Farms in the United Kingdom and Denmark* (the Renewable Energy Foundation, 2012).

Guo, H., Xu, M. & Hu, Q. Changes in near-surface wind speed in China: 1969-2005. *Int. J. Climatol.* **31**, 349-358 (2011).

Wu, J., Zha, J. L., Zhao, D. M. & Yang, Q. D. Changes of wind speed at different heights over Eastern China during 1980-2011. *Int. J. Climatol.* **38**, 4476-4495 (2018).

Additional information

Supplementary information is available in the online version of the paper. Reprints and permissions information is available online at www.nature.com/reprints.

Correspondence and requests for materials should be addressed to Z. Zeng.

Acknowledgements

This study was supported by Lamsam-Thailand Sustain Development (B0891). L. Li was partially supported by the National Key Research and Development Program of China (Grant-2018YFC1507704). J. Liu was supported by the National Natural Science Foundation of China (41625001). We thank Della Research Computing in Princeton University for providing computing resources. We thank the U.S. National Climatic Data Center and the U.K. Met Office Hadley Centre for providing surface wind speed measurements, and thank the Program for Climate Model Diagnosis and Intercomparison and the IPSL Dynamic Meteorology Laboratory for providing surface wind speed simulations.

Author contributions

Z. Zeng and E. Wood designed the research. Z. Zeng and L. Yang performed analysis; Z. Zeng, A. Ziegler, T. Searchinger wrote the draft; and all the authors contributed to the interpretation of the results and the writing of the paper.

Data availability. The data for quantifying wind speed changes are the Global Surface Summary of the Day database (GSOD, ftp://ftp.ncdc.noaa.gov/pub/data/gsod), and the HadISD (version v2.0.2.2017f) global sub-daily database (https://www.metoffice.gov.uk/hadobs/hadisd/). The

time series of climate indices describing monthly atmospheric and oceanic phenomena are obtained from the National Oceanic and Atmospheric Administration (https://www.esrl.noaa.gov/psd/data/climateindices/list/). Simulated wind speed changes in Coupled Model Intercomparison Project Phase 5 (CMIP5) are available in the Program for Climate Model Diagnosis and Intercomparison (https://esgf-node.llnl.gov/projects/cmip5/). Simulated wind speed changes constrained by historical sea surface temperature are provided by the IPSL Dynamic Meteorology Laboratory. Wind records in reanalysis products include the ECMWF ERA-Interim Product (apps.ecmwf.int/datasets/data/interim-full-daily/), the ECMWF ERA5 Product (https://cds.climate.copernicus.eu/cdsapp#!/dataset/reanalysis-era5-single-levels-monthly-means) and the NCEP/NCAR Global Reanalysis Product (http://rda.ucar.edu/datasets/ds090.0/). The processed wind records and the relevant code are available in Supplementary Data 1 and 2. All datasets are also available on request from Z. Zeng.

Code availability. The program used to generate all the results is MATLAB (R2014a) and ArcGIS (10.4). Analysis scripts are available by request from Z. Zeng. The code producing wind records are available in Supplementary Data 1 and 2.

Competing financial interests

The authors declare no competing financial interests.

445 **Figure Legends.**

446 **Figure 1. Turning point for mean global surface wind speed (*u*).** (**a**) Global mean annual *u*
447 during 1978-2017 (black dot and line). The piecewise linear regression model indicates a
448 statistically significant turning point in 2010. The red line is the piecewise linear fit (R^2 = 90%, P
449 < 0.001). The dashed line indicates the turning point. The trends before and after the turning
450 point are shown in the inset. Each grey line (n = 300) is a piecewise linear fit for a randomly
451 selected subset (40%) of the global stations. (**b**) Frequency distribution of the estimated turning
452 points derived from the 300 resampling results. (**c**) Frequency distribution of the trends in mean
453 annual *u* before and after the turning point from the 300 resampling results. The result is based
454 on the weather stations in the GSOD database.

455 **Figure 2. Factors driving the decadal variations in *u*.** Observed (black) and reconstructed (red)
456 detrended mean annual *u* over the following: (a) the globe, (b) North America, (c) Europe, and (d)
457 Asia. The models are trained only using the detrended time series before the turning points. The
458 dashed line indicates the turning point (2010 for the globe, 2012 for North America, 2003 for
459 Europe, and 2001 for Asia). For the globe and each of the three continents, we select six largest
460 explanatory climate indices for the decadal variations of *u* with a stepwise forwarding regression
461 model. The selected climate indices are then used to reconstruct decadal variations of *u* via a
462 multiple regression. Uncertainties are the inter-quartile range of the results based on a randomly
463 selected 40% subset of the station pools (repeated 300 times). Inset plots indicate the locations of
464 the stations. Inset black numbers are coefficients of determination between observed and
465 reconstructed *u* before the turning points. Inset red numbers are correlation coefficient and its
466 significance between observed and reconstructed *u* after the turning points.

Figure 3. Mechanisms for the decadal variation in *u*. Normalized mean annual surface temperature for the years with negative (**a**) and positive (**b**) anomalies of detrended wind. Characteristic regions for Pacific Decadal Oscillation (PDO), North Atlantic Oscillation (NAO) and Tropical Northern Atlantic Index (TNA) are outlined by green, red, and blue boxes, respectively. Surface temperature over land is obtained from Climate Research Unit TEM4 with a spatial resolution of 5° by 5° (ref. 50), and that over ocean is from NOAA Optimum Interpolation (OI) Sea Surface Temperature V2, with a spatial resolution of 1° by 1° (ref. 51). Spatial patterns of the correlation between the regional ($5^o \times 5^o$) mean annual *u* and the following: (**c**) TNA; (**d**) NAO; and (**e**) PDO for 1978-2017. Dotting represents significant at $P < 0.05$ level. Decadal variations are shown in panels (**f**) for TNA and regional *u* in North America; (**g**) for NAO and regional *u* in Europe; and (**h**) for PDO and regional *u* in Asia. The thin lines are annual values; and the thick lines are 9-year-window moving averages. The black lines are wind speed; and each of the colored lines are TNA, NAO, and PDO, respectively.

Figure 4. Implications of the recent reversal in global terrestrial stilling for wind energy industry. (**a**) Frequency distribution of global average hourly *u* in 2010 and 2017, and the year 2024 assuming the same increasing rate. (**b**) Time series of the overall capacity factor for wind generation in the U.S. (black line) and the three-order of the regional-average *u* (u^3; blue line) from 2008 to 2017. The inset scatter plot shows the significant relationship between the overall capacity factor and the regional u^3 ($R = 0.86$, $P < 0.01$). The inset black numbers show the trend in the overall capacity factor for wind generation, and the inset red numbers show the *u*-induced increase of capacity factor in the U.S.. (**c**) Mean annual *u* observed at a weather station near an installed turbine at Deaf Smith County, the U.S. (<1 km). The inset plot shows the location. The turbine was installed in 2014. The background colors separate different periods: P0, the 1980s

level when *u* is relative strong (1978-1995); P1, the evaluation years before the installation of the turbine (2009-2013); P2, the operation years when the turbine is generating power (2014-2017). (**d**) Mean annual wind power production at Deaf Smith County, the U.S. from different wind turbines during different periods (grey: General Electric GE 1.85 – 87; green: General Electric GE 2.5 – 120 turbine; blue: the theoretical maximum ratio of power that can be extracted by a wind turbine given diameter of 120 m and hub height of 120 m). Error bars show the interannual variability within the periods.

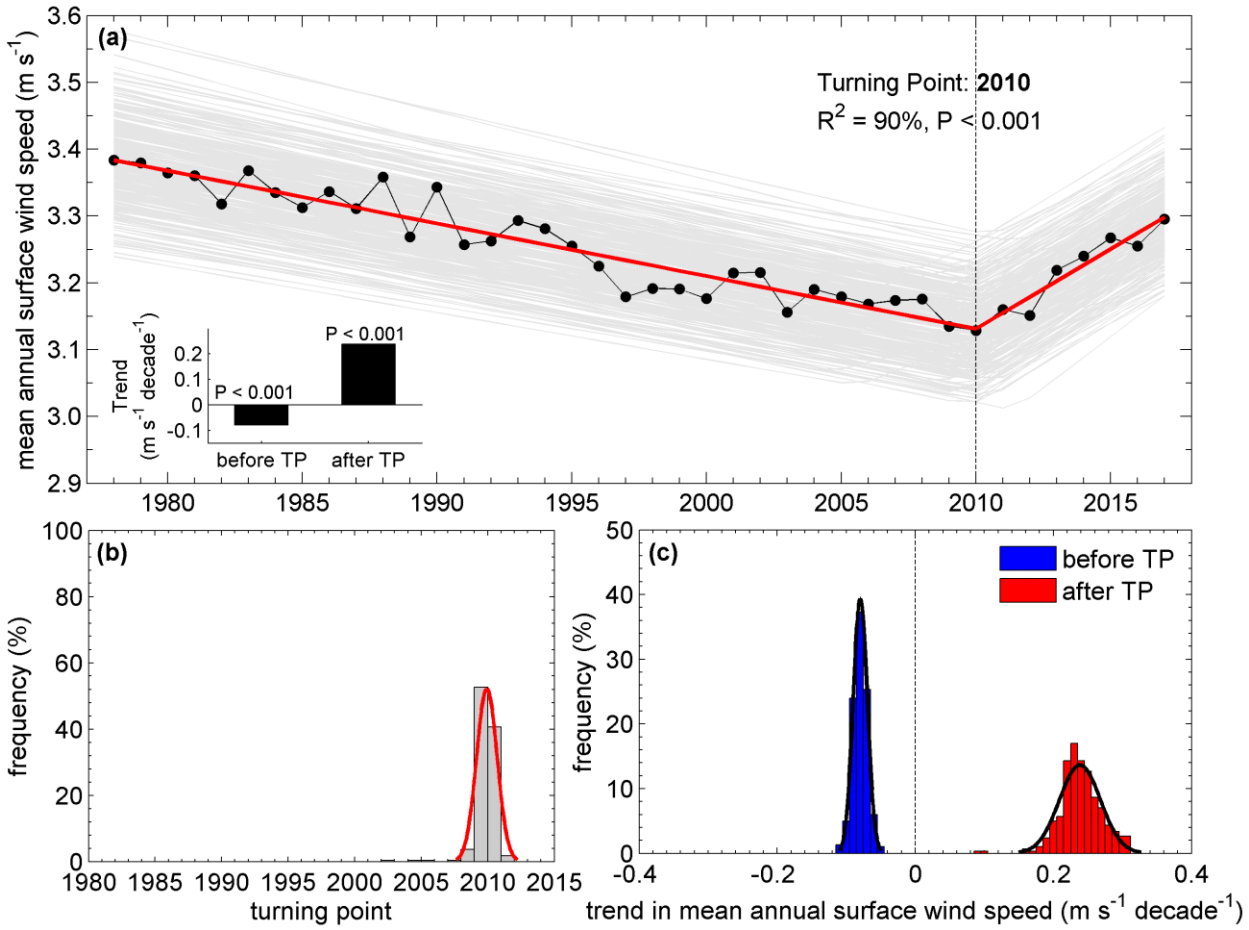

Figure 1. Turning point for mean global surface wind speed (*u*). (**a**) Global mean annual *u* during 1978-2017 (black dot and line). The piecewise linear regression model indicates a statistically significant turning point in 2010. The red line is the piecewise linear fit (R^2 = 90%, P < 0.001). The dashed line indicates the turning point. The trends before and after the turning point are shown in the inset. Each grey line (n = 300) is a piecewise linear fit for a randomly selected subset (40%) of the global stations. (**b**) Frequency distribution of the estimated turning points derived from the 300 resampling results. (**c**) Frequency distribution of the trends in mean annual *u* before and after the turning point from the 300 resampling results. The result is based on the weather stations in the GSOD database.

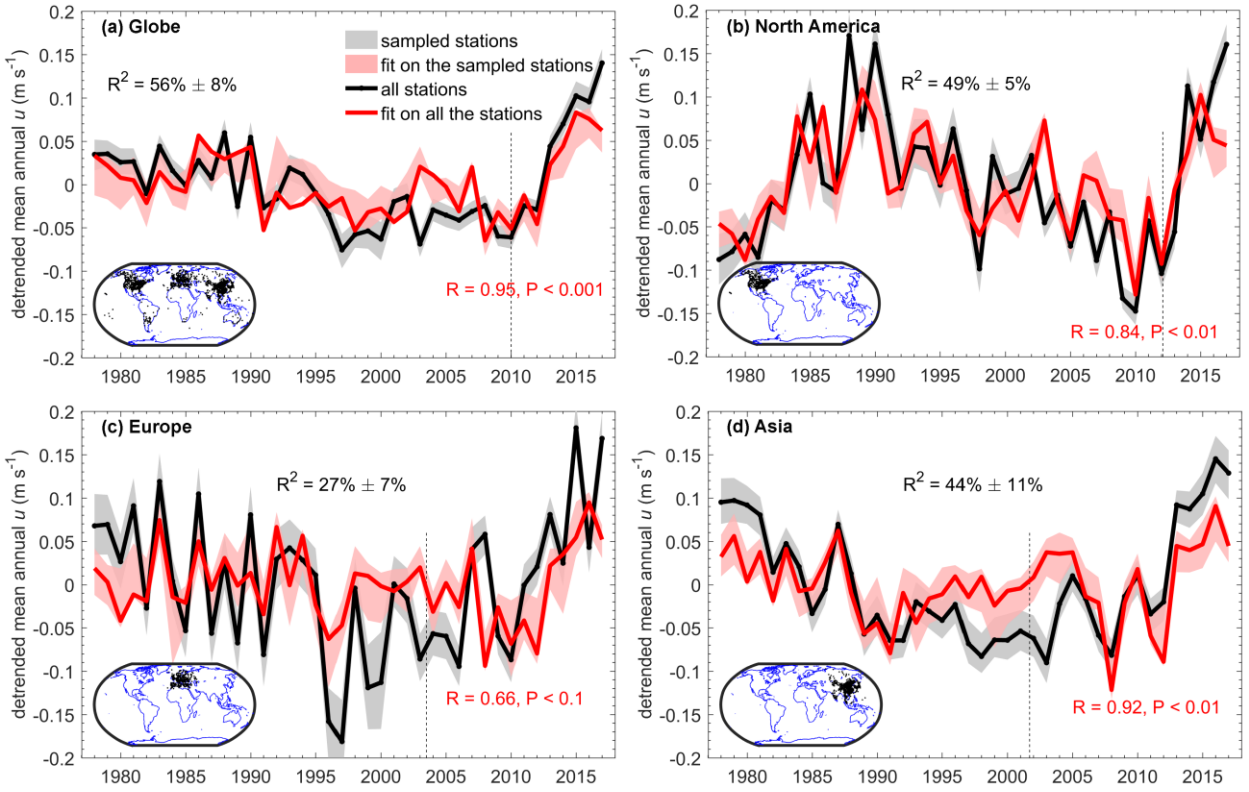

Figure 2. Factors driving the decadal variations in *u*. Observed (black) and reconstructed (red) detrended mean annual *u* over the following: (**a**) the globe, (**b**) North America, (**c**) Europe, and (**d**) Asia. The models are trained only using the detrended time series before the turning points. The dashed line indicates the turning point (2010 for the globe, 2012 for North America, 2003 for Europe, and 2001 for Asia). For the globe and each of the three continents, we select six largest explanatory climate indices for the decadal variations of *u* with a stepwise forwarding regression model. The selected climate indices are then used to reconstruct decadal variations of *u* via a multiple regression. Uncertainties are the inter-quartile range of the results based on a randomly selected 40% subset of the station pools (repeated 300 times). Inset plots indicate the locations of the stations. Inset black numbers are coefficients of determination between observed and reconstructed *u* before the turning points. Inset red numbers are correlation coefficient and its significance between observed and reconstructed *u* after the turning points.

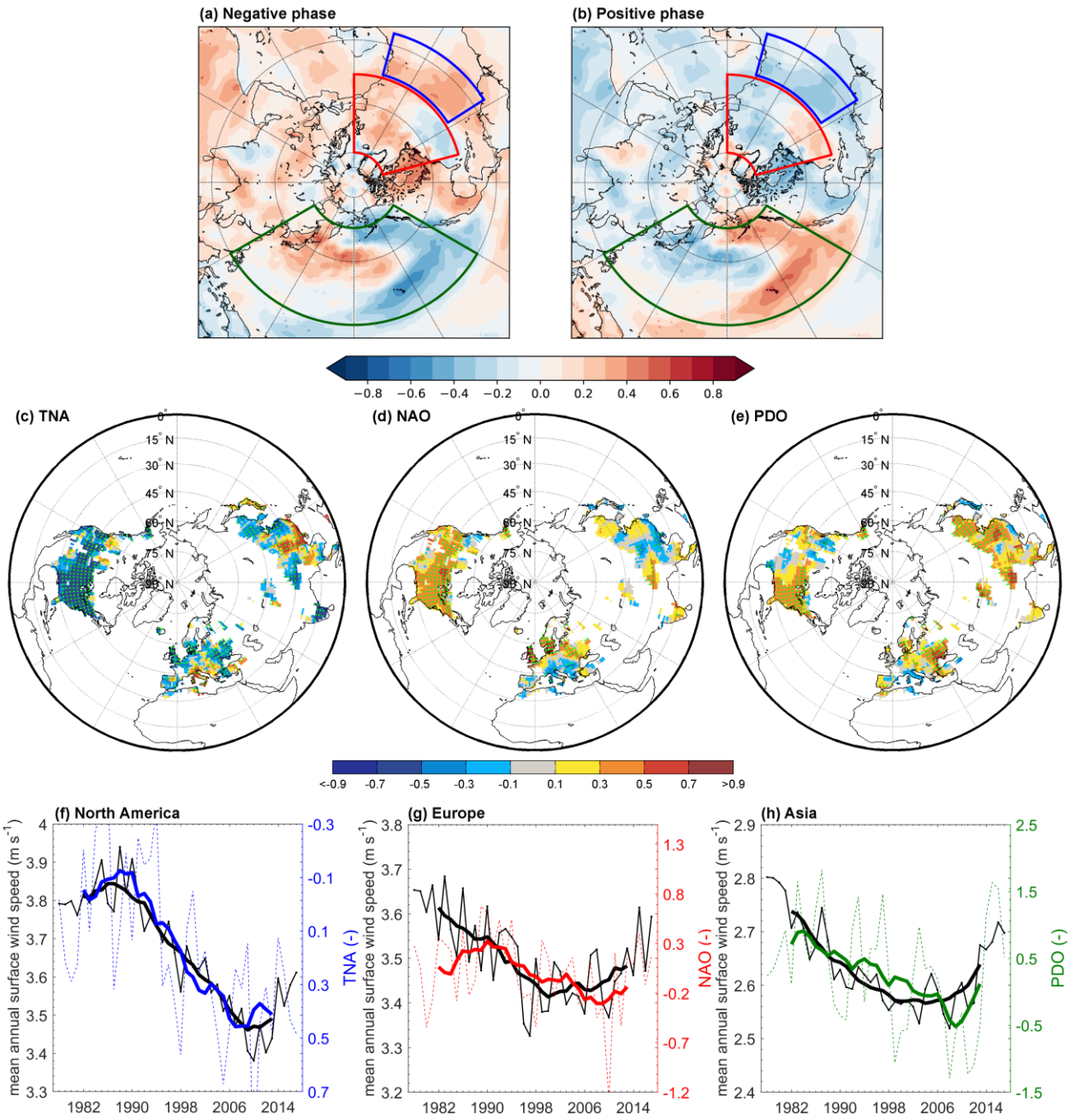

519 **Figure 3. Mechanisms for the decadal variation in *u*.** Normalized mean annual surface
520 temperature for the years with negative (**a**) and positive (**b**) anomalies of detrended wind.
521 Characteristic regions for Pacific Decadal Oscillation (PDO), North Atlantic Oscillation (NAO)
522 and Tropical Northern Atlantic Index (TNA) are outlined by green, red, and blue boxes,
523 respectively. Surface temperature over land is obtained from Climate Research Unit TEM4 with

a spatial resolution of 5° by 5° (ref. 50), and that over ocean is from NOAA Optimum Interpolation (OI) Sea Surface Temperature V2, with a spatial resolution of 1° by 1° (ref. 51). Spatial patterns of the correlation between the regional ($5^o \times 5^o$) mean annual *u* and the following: (**c**) TNA; (**d**) NAO; and (**e**) PDO for 1978-2017. Dotting represents significant at $P < 0.05$ level. Decadal variations are shown in panels (**f**) for TNA and regional *u* in North America; (**g**) for NAO and regional *u* in Europe; and (**h**) for PDO and regional *u* in Asia. The thin lines are annual values; and the thick lines are 9-year-window moving averages. The black lines are wind speed; and each of the colored lines are TNA, NAO, and PDO, respectively.

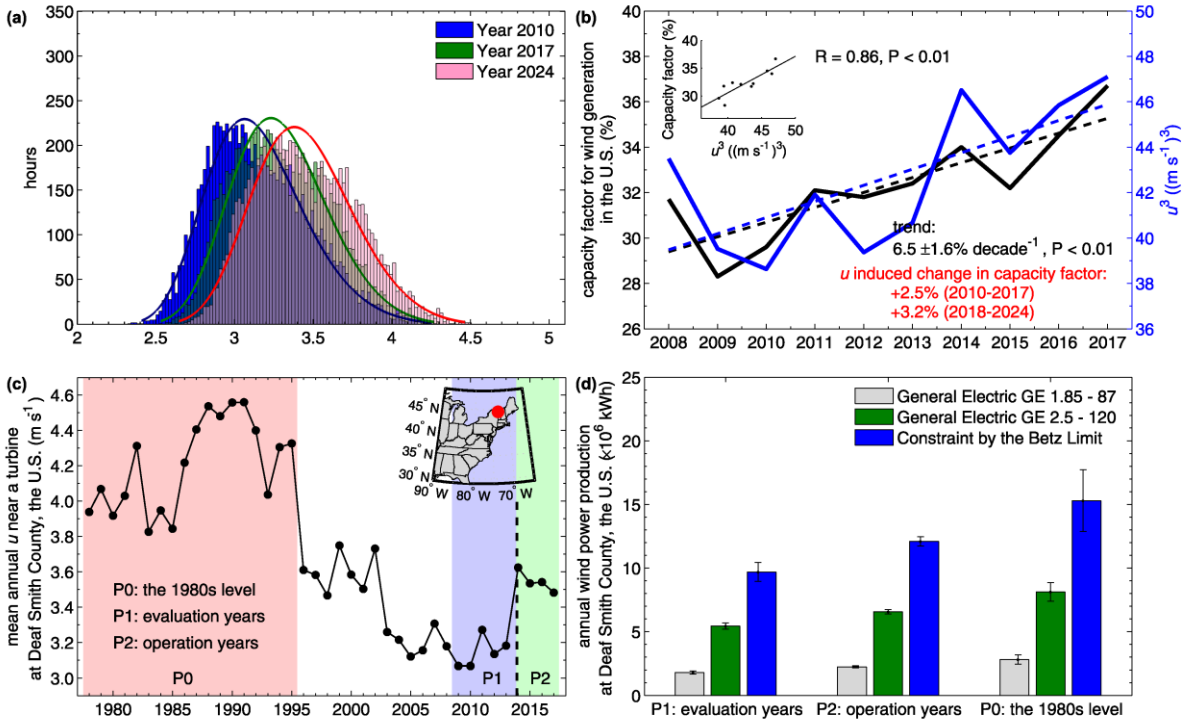

Figure 4. Implications of the recent reversal in global terrestrial stilling for wind energy industry. (**a**) Frequency distribution of global average hourly *u* in 2010 and 2017, and the year 2024 assuming the same increasing rate. (**b**) Time series of the overall capacity factor for wind generation in the U.S. (black line) and the three-order of the regional-average *u* (u^3; blue line) from 2008 to 2017. The inset scatter plot shows the significant relationship between the overall capacity factor and the regional u^3 (R = 0.86, P < 0.01). The inset black numbers show the trend in the overall capacity factor for wind generation, and the inset red numbers show the *u*-induced increase of capacity factor in the U.S.. (**c**) Mean annual *u* observed at a weather station near an installed turbine at Deaf Smith County, the U.S. (<1 km). The inset plot shows the location. The turbine was installed in 2014. The background colors separate different periods: P0, the 1980s level when *u* is relative strong (1978-1995); P1, the evaluation years before the installation of the turbine (2009-2013); P2, the operation years when the turbine is generating power (2014-2017). (**d**) Mean annual wind power production at Deaf Smith County, the U.S. from different wind

545 turbines during different periods (grey: General Electric GE 1.85 – 87; green: General Electric
546 GE 2.5 – 120 turbine; blue: the theoretical maximum ratio of power that can be extracted by a
547 wind turbine given diameter of 120 m and hub height of 120 m). Error bars show the interannual
548 variability within the periods.